

# Time-resolved turbulent velocity field reconstruction using a long short-term memory (LSTM)-based artificial intelligence framework

Cite as: Phys. Fluids 31, 075108 (2019); <https://doi.org/10.1063/1.5111558>

Submitted: 27 May 2019 . Accepted: 26 June 2019 . Published Online: 25 July 2019

Zhiwen Deng (邓志文), Yujia Chen (陈宇佳), Yingzheng Liu (刘应征) , and Kyung Chun Kim (김경천) 



View Online



Export Citation



CrossMark



CAPTURE WHAT'S POSSIBLE  
WITH OUR NEW PUBLISHING ACADEMY RESOURCES

[Learn more](#) 

AIP Publishing

# Time-resolved turbulent velocity field reconstruction using a long short-term memory (LSTM)-based artificial intelligence framework

Cite as: Phys. Fluids 31, 075108 (2019); doi: 10.1063/1.5111558

Submitted: 27 May 2019 • Accepted: 26 June 2019 •

Published Online: 25 July 2019



Zhiwen Deng (邓志文),<sup>1,2,3</sup> Yujia Chen (陈宇佳),<sup>1,3</sup> Yingzheng Liu (刘应征),<sup>1,3</sup> and Kyung Chun Kim (김경천)<sup>2,a)</sup>

## AFFILIATIONS

<sup>1</sup>Key Lab of Education Ministry for Power Machinery and Engineering, School of Mechanical Engineering, Shanghai Jiao Tong University, 800 Dongchuan Road, Shanghai 200240, China

<sup>2</sup>Experimental Thermo-Fluids Mechanics and Energy Systems (ExTENsys) Laboratory, Pusan National University, Busandaehak-ro 63beon-gil, Geumjeong-gu, Busan 46241, South Korea

<sup>3</sup>Gas Turbine Research Institute, Shanghai Jiao Tong University, 800 Dongchuan Road, Shanghai 200240, China

<sup>a)</sup>Author to whom correspondence should be addressed: kckim@pusan.ac.kr

## ABSTRACT

This paper focuses on the time-resolved turbulent flow reconstruction from discrete point measurements and non-time-resolved (non-TR) particle image velocimetry (PIV) measurements using an artificial intelligence framework based on long short-term memory (LSTM). To this end, an LSTM-based proper orthogonal decomposition (POD) model is proposed to establish the relationship between velocity signals and time-varying POD coefficients obtained from non-TR-PIV measurements. An inverted flag flow at  $Re = 6200$  was experimentally measured using TR-PIV at a sampling rate of 2000 Hz for the construction of training and testing datasets and for validation. Two different time-step configurations were employed to investigate the robustness and learning ability of the LSTM-based POD model: a single-time-step structure and a multi-time-step structure. The results demonstrate that the LSTM-based POD model has great potential for time-series reconstruction since it can successfully recover the temporal evolution of POD coefficients with remarkable accuracy, even in high-order POD modes. The time-resolved flow fields can be reconstructed well using coefficients obtained from the proposed model. In addition, a relative error reconstruction analysis was conducted to compare the performance of different time-step configurations further, and the results demonstrated that the POD model with multi-time-step structure provided better reconstruction of the flow fields.

Published under license by AIP Publishing. <https://doi.org/10.1063/1.5111558>

## NOMENCLATURE

$a_i(t)$	coefficient of the $i$ th POD mode	$i_t$	the input gate of an LSTM cell
$b$	bias vectors of an LSTM cell	$H$	width of the inverted flag (mm)
$C_t$	state of an LSTM cell	$K_B$	dimensionless bending stiffness
$\tilde{C}_t$	updated state of an LSTM cell	$L$	length of the inverted flag (mm)
$N$	number of the first POD modes	$o_t$	the output gate of an LSTM cell
$N_t$	total number of POD modes	$P$	ensemble covariance matrix of systematic samples
$f_0$	flapping frequency of the inverted flag (Hz)	$R_{uu}(x, x')$	the two-point correlation matrix
$f_f$	the forget gate of an LSTM cell	$Re$	Reynolds number based on the length of the inverted flag
$f_p$	sampling rate of non-time-resolved PIV measurement (Hz)	$t$	time
$h$	thickness of the inverted flag (mm)	$t^*$	nondimensional time, $t^* = tU_0/L$
$h_t$	the output of an LSTM cell	$U$	weight matrices of an LSTM cell
		$U^*$	dimensionless streamwise velocity normalized by min-max normalization

$U_0$	average velocity of the free stream ( $\text{m s}^{-1}$ )
$u$	streamwise velocity ( $\text{m s}^{-1}$ )
$u_l$	velocity reconstructed using real POD coefficients ( $\text{m s}^{-1}$ )
$u_p$	velocity estimated using the LSTM artificial intelligence framework ( $\text{m s}^{-1}$ )
$W$	weight matrices of an LSTM cell
$x_t$	the input of an LSTM cell
$X^*$	streamwise coordinate normalized by $L$
$Y^*$	wall-normal coordinate normalized by $L$

### Greek symbols

$\lambda$	eigenvalue
$\phi$	eigenmode of proper orthogonal decomposition
$\varepsilon_r$	relative reconstruction error
$\eta_i$	energy-containing percent in the $i$ th POD mode

### Abbreviations

MTD-mLSE	multi-time-delay modified linear stochastic estimation
LSTM	long short-term memory
TKE	turbulence kinetic energy
TR-PIV	time-resolved particle image velocimetry
POD	proper orthogonal decomposition
ROM	reduced-order model

## I. INTRODUCTION

The pursuit of flow field data with high temporal resolution has been one of the major concerns in fluid mechanics. It is generally accepted that time-resolved data are essential to elucidate the flow dynamics fully, including identification and evolution of vortex and deep analysis using dynamic mode decomposition (DMD).<sup>1</sup> With faster developments in state-of-the-art time-resolved particle image velocimetry (TR-PIV) and high-frequency hotwires, more and more intricate and finer flow structures in time scales can be obtained. However, a system of high-repetition TR-PIV usually requires very-high-speed cameras and high-powered lasers, which are very expensive and thus unavailable sometimes. Alternatively, powerful machine learning techniques have huge potential for temporal and spatial resolution enhancement of flow fields<sup>2,3</sup> and are attracting increasing attention in fluid mechanics.<sup>4–7</sup> The development of an efficient machine-learning-based time-resolved flow reconstruction technology is highly desirable.

Considerable research efforts have been devoted to augmenting the temporal resolution of non-time-resolved (non-TR) flow fields in order to assess the evolution of flow structures, especially for some unsteady flows at high Reynolds number. Tu *et al.*<sup>8</sup> proposed a three-step method based on multi-time-delay modified linear stochastic estimation (MTD-mLSE) and a Kalman smoother. In this approach, the time-varying coefficients of proper orthogonal decomposition (POD) were estimated using a time-resolved point measurement signal. Thus, non-TR-PIV measurements (32 Hz) and TR velocity sensors (800 Hz) were successfully integrated to estimate the velocity fields dynamically for flow over a flat plate. However, the temporal enhancement is limited due to the restrictions

of the LSE-based approach. Romain *et al.*<sup>9</sup> reconstructed the time-resolved flow fields of an airfoil with indirect point measurements of a voltage signal obtained from hot-film sensors and non-TR-PIV measurements. They used regression models and an ensemble Kalman filter (EnKF)-based POD reduced-order model (ROM). This flow-reduced model was assessed by applying the Galerkin projection of the Navier-Stokes equation. The results showed that the regression models have better performance with a much lower relative error than the MTD-mLSE model. Despite its good performance with the regression models and EnKF, the method was subject to the defects inherent to the Galerkin projection-based ROM, which is nonrobust and structurally unstable. He and Liu<sup>10</sup> developed a general POD-based spatial refinement approach that combined high-spatial-resolution non-TR-PIV with low-spatial-resolution TR-PIV to increase the spatial resolution of TR-PIV. They evaluated the approach using a free round jet flow at a Reynolds number of 3000. Nevertheless, their approach was based on least-square estimation, and they leveraged the whole time-resolved PIV data to recover the time-resolved POD coefficients.

For some particular flows, the mentioned approaches can successfully enhance the temporal or spatial resolution of PIV measurements by recovering time-resolved POD coefficients based on linear or regression models. However, surprisingly little attention has been devoted to combining powerful deep learning algorithms with POD analysis. In order to predict the high-dimensional quantities, such as pressure, temperature, and strain fields, Swischuk *et al.*<sup>11</sup> successfully established the mapping between physical characteristics (such as Mach number and lift coefficients) and POD coefficients using four different machine learning algorithms—neural networks, multivariate polynomial regression, k-nearest-neighbors, and decision trees. The results showed great potential to combine the machine learning algorithms with POD. Mohan and Gaitonde<sup>12</sup> proposed an approach based on long short-term memory (LSTM) to build a POD-ROM without using Galerkin projection for turbulent flow control. They trained the networks with DNS-based data and predicted the changing tendency of POD coefficients using the history values of coefficients with an LSTM neural network, which is applicable to time-series data. However, to the best of our knowledge, there has been no systematic combination of an LSTM-based approach coupled with discrete velocity signals and POD coefficients in experimental fluid dynamics.

The present study proposes an LSTM-based POD model that can establish a relationship between time-varying POD coefficients and discrete point velocity signals to reconstruct time-resolved flow fields and then enhance the temporal resolution of turbulent flow. To this end, an inverted flag flow<sup>13</sup> in flapping mode with a Reynolds number  $Re = 6200$  was selected as a benchmark configuration to demonstrate the reliability of the approach. The time-resolved velocity fields obtained by TR-PIV at a sampling rate of 2000 Hz were applied to extract high-frequency discrete point velocity signals and used for validation.

The LSTM-based POD model was first trained with non-TR datasets at a sampling rate of 5 Hz, which were obtained by down-sampling the time-resolved flow fields. This model can provide a faithful reconstruction of the temporal evolution of velocity flow fields at 2000 Hz. Particular attention is given to the influence of different structures on the performance of the LSTM-based model:

a model with a multi-time-step structure and one with a single-time-step structure. This approach could also be readily modified for turbulent flow control.

## II. MATHEMATICAL FUNDAMENTALS

### A. Proper orthogonal decomposition

Proper orthogonal decomposition (POD) is also known as principle component analysis or singular system analysis and is widely used in fluid mechanics to extract larger-scale or coherent structures in various flow configurations.<sup>14</sup> Detailed information regarding the mathematical fundamentals of POD is available from Lumley<sup>15</sup> and Sirovich.<sup>16</sup> The general motivation of POD analysis is to find the optimal representation of flow field realizations by extracting the most energetic eigenmodes that capture most of the fluctuation energy. This optimization problem is equivalent to solving the following Fredholm integral eigenvalue equation:<sup>10,14,16,17</sup>

$$\int R_{uu}(x, x') \phi_i(x') dx' = \lambda_i \phi_i(x), \quad (1)$$

$\phi_i(x)$  is the  $i$ th eigenfunction and is also known as the  $i$ th POD mode.  $\lambda_i$  is the  $i$ th eigenvalue and represents the amount of kinetic energy contained in corresponding mode  $\phi_i(x)$ .  $R_{uu}(x, x')$  is a two-point correlation matrix that is calculated using a sequence of instantaneous flow fields,

$$R_{uu}(x, x') = \langle u(x, t) u^*(x', t) \rangle, \quad (2)$$

where  $\langle \dots \rangle$  is the ensemble average operator and the superscript \* denotes the complex conjugate. The  $i$ th coefficient  $a_i(t)$  of the corresponding POD mode can be calculated from

$$a_i(t) = \int u(x, t) \phi_i(x) dx. \quad (3)$$

The first  $N$ th POD modes usually capture most of the energy and large flow structures in a turbulent flow. Thus, each instantaneous fluctuating field can be reconstructed using the first  $N$ th POD modes in a linear combination as

$$u(x, t) = \sum_{i=1}^N a_i(t) \phi_i(x). \quad (4)$$

As demonstrated in Eq. (4), a spatiotemporal velocity field can generally be decomposed into two independent parts: POD modes reflecting spatial characteristics and time-varying coefficients reflecting temporal characteristics. This indicates the importance of recovering POD coefficients for improving temporal resolution in turbulent flows.

### B. Long short-term memory neutral networks

LSTM neural networks were first introduced by Hochreiter.<sup>18</sup> They have since been improved and are popular in different fields, such as speech recognition,<sup>19</sup> language translation,<sup>20</sup> and time series prediction.<sup>21</sup> As a special type of artificial recurrent neural network (RNN), LSTM networks were designed to mitigate the exploding and vanishing gradient problems in the training process of traditional RNNs.<sup>22</sup> LSTM networks have great learning ability in addressing classifying or regression problems based on time-series data because of their special network architecture and feedback connections.

The basic architecture of LSTM neutral networks is shown in Fig. 1. Each LSTM cell is generally composed of three multiplicative gates: the input, output, and forget gates. These gates allow the LSTM memory cell to store and obtain information over long periods of time, thereby attenuating the problems of a vanishing gradient. Intuitively, the forget gate is responsible for discarding or retaining the information, which is similar to the memory function in the human brain. The LSTM transition equations at each time step  $t$  can be calculated as follows:<sup>12</sup>

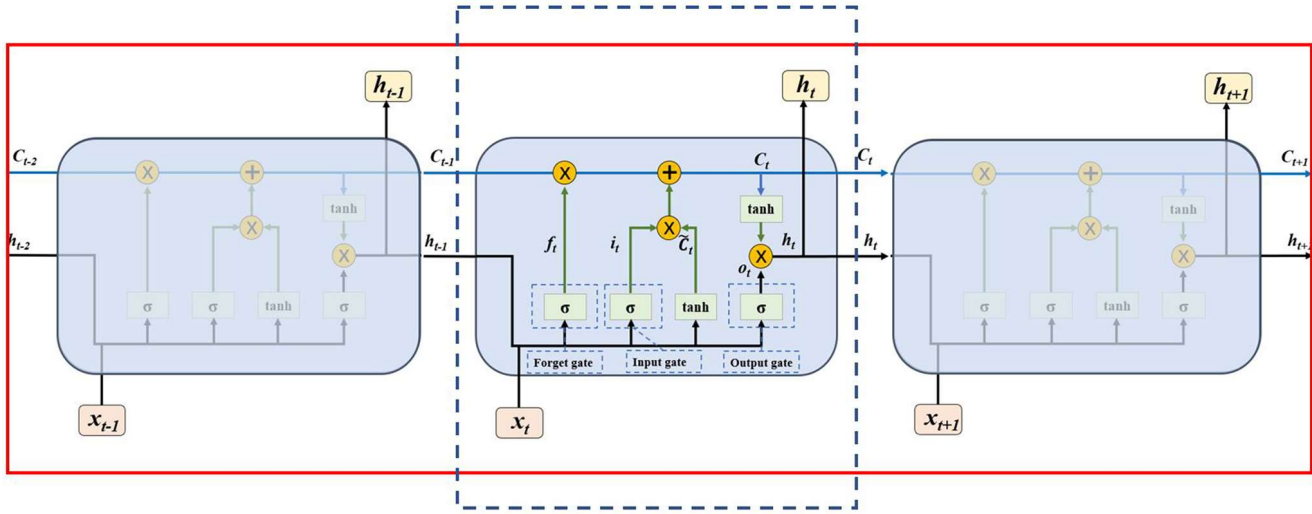


**FIG. 1.** Basic architecture of the LSTM network. The blue dashed rectangle denotes the structure of the single-time-step LSTM model, while the red dashed rectangle denotes the structure of the multi-time-step LSTM model.

$$i_t = \sigma(W_i x_t + U_i h_{t-1} + b_i), \quad (5)$$

$$f_t = \sigma(W_f x_t + U_f h_{t-1} + b_f), \quad (6)$$

$$\tilde{C}_t = \tanh(W_c x_t + U_c h_{t-1} + b_c), \quad (7)$$

$$C_t = i_t \otimes \tilde{C}_t + f_t \otimes C_{t-1}, \quad (8)$$

$$o_t = \sigma(W_o x_t + U_o h_{t-1} + b_o), \quad (9)$$

$$h_t = o_t \otimes \tanh(C_t), \quad (10)$$

where  $x_t$  is the cell input and  $h_t$  is the cell output.  $f_t$ ,  $i_t$ , and  $o_t$  denote the forget gate, input gate, and output gate, respectively. The entries of the gating vector  $f_t$ ,  $i_t$ , and  $o_t$  are between 0 (gate closed) and 1 (gate open).  $C_t$  represents the cell state, while  $\tilde{C}_t$  represents the updated cell state. The  $W$  and  $U$  terms are weight matrices of different gates, and the  $b$  terms are bias vectors. These weights and biases need to be learned from the training process.  $\sigma$  is the logistic sigmoid function, and  $\otimes$  is the operator of element-wise multiplication.

A global view of the data flow in Fig. 1 shows that the states are propagated forward through the network. Similar to traditional RNNs, LSTM is also a differential function approximator that can be trained with a gradient descent algorithm, and the error gradients are back-propagated in the opposite direction of data flow. More detailed information regarding LSTM is available from Graves.<sup>22</sup>

In this study, the LSTM network is employed as a bridge to establish a relationship between two different temporal sequences: the discrete velocity signals and the coefficients in different POD modes. Two different kinds of configurations were applied to investigate the robustness of the LSTM-based artificial framework: single-time-step and multi-time-step configurations. In Fig. 1, the blue dashed rectangle denotes the single-time-step structure, while the red solid rectangle denotes the multi-time-step structure.

### C. Overview of the method

A flow chart of the proposed strategy is shown in Fig. 2. The general goal in this work is to combine non-TR-PIV measurements and time-resolved point measurements to reconstruct time-resolved

global flow fields. The implementation of this strategy can be divided into three steps:

- (a) First, sufficient non-TR-PIV data measurements are collected synchronously with time-resolved velocity signals. The POD procedure is then performed on the flow fields obtained by non-TR-PIV and yields a set of POD modes and non-TR coefficients. The non-TR velocity signals can be accessed by downsampling the original TR signals at the same sampling frequency and time steps with the PIV. After that, the non-TR dataset can be established by pairing each set of POD coefficients with its corresponding velocity signals.
- (b) Second, a machine-learning-based model is built to learn the relationship between velocity signals and POD coefficients and trained with the non-TR dataset. The non-TR velocity signals serve as the input of model, while the coefficients are the output.
- (c) Third, the time-resolved POD coefficients are estimated by leveraging the trained ML model with time-resolved velocity signals as an input. The test samples should be resampled to have the same frequency as the training samples since the LSTM-based POD model only establishes the relationship at low frequency. After that, the time-resolved global flow fields can be reconstructed using time-resolved coefficients and their corresponding modes. The flow field recovered using the first  $N$ th POD modes merely contains the most energetic part of the truth flow but is actually still a kind of reduced-order flow field.

Particular emphasis is placed on developing a robust and advanced machine learning model that can be used to establish the relationship between these two temporal sequences. The LSTM-based POD model is readily established by combining the discrete velocity signals and the POD mode coefficients. In general, this problem can be essentially regarded as a regression problem of a temporal-sequence learning. The whole architecture of the LSTM-based POD model is shown in Fig. 3. The red points on the velocity signal match with the visible non-TR-PIV measurements, whereas the gray points match with invisible flow fields, which need to be reconstructed from the LSTM-based POD model. The mean-squared error between real POD coefficients and model outputs was selected as a loss function since the problem is a regression problem. Given the input velocity signals and their corresponding output POD coefficients, the aim of the LSTM network is to seek the optimal weights and biases to minimize the loss function.

The specific data flow procedure can be summarized as follows. First, the original input velocity signals pass through the data preprocessing procedure to eliminate the influence of singular sample data. (More detailed information regarding data preprocessing will be discussed in Secs. III B and III C.) After that, the data are fed into the first LSTM layer for training. Subsequently, a batch normalization layer,<sup>23</sup> which can fix the means and variances of each layer's inputs within a certain range, is employed to accelerate the training process of deep networks. It can also play a role as a regularizer to mitigate the problem of overfitting and improve the generalization ability of the neural networks. Finally, the second LSTM layer and a dense<sup>24</sup> layer (the dense layer is the regular densely connected neural network layer, and it helps to map the features learned from the previous layers onto the output space) are applied to have a deeper

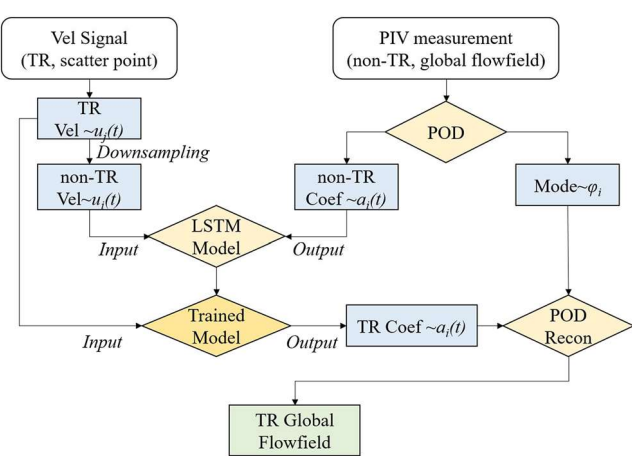


**FIG. 2.** Flow chart of the strategy for reconstructing time-resolved flow fields using the LSTM-based model.

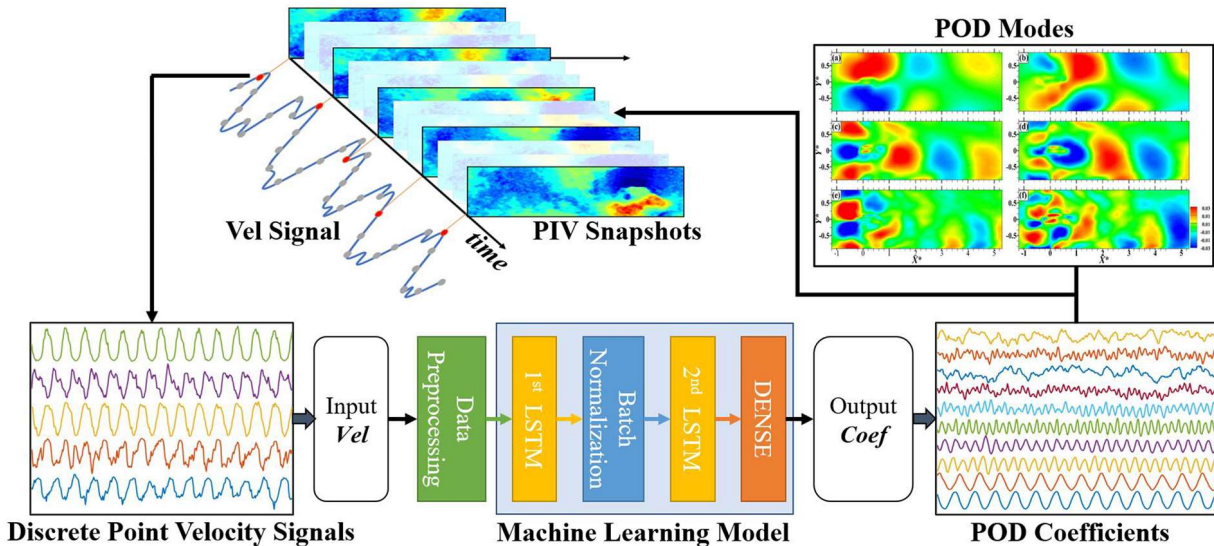


FIG. 3. The whole architecture of the LSTM-based POD model.

network architecture that has the potential to improve the network's performance substantially by allowing modeling mappings of complexity.<sup>25</sup>

In contrast to the direction of data flow, the gradients of the error were back-propagated through the whole neural network to train the weights and biases of the network. An adaptive moment estimation (Adam) optimizer<sup>26</sup> was leveraged in this algorithm and provided good performance. Five LSTM-based POD models containing the first 50 POD coefficients in total were applied simultaneously in this study. Each LSTM-based POD model containing outputs of 10 coefficients was trained with 5000 training epochs. The training error curve was set as a criterion for convergence. Additionally, single and multi-time-step configurations were employed. The open-source code Tensorflow<sup>27</sup> and Keras<sup>28</sup> based on Python were used in the design and implementation of the LSTM-based POD model.

### III. EXPERIMENTAL SETUP

#### A. Experimental apparatus

The experimental data used in the present study were previously obtained by Yu *et al.*<sup>13</sup> The experiment was conducted in a water tunnel with a test section of size of 40 mm (width)  $\times$  80 mm (height)  $\times$  900 mm (length), as shown in Fig. 4(a). An inverted flag was clamped by a transparent plate at the trailing edge and installed vertically in the middle plane of the test section. The flag was made of transparent polyethylene terephthalate with a length  $L$  of 20 mm, width  $H$  of 60 mm, and thickness  $h$  of 100  $\mu\text{m}$ . The inverted flag flow at  $\text{Re} = 6200$  (based on  $L$  and the free stream velocity  $U_0$ ) was selected as a benchmark to investigate the performance of the LSTM-based POD model. This flow configuration is worth studying because the dimensionless bending stiffness  $K_B$  of the inverted flag is 0.28, and the flag oscillates strongly in flapping

mode, which indicates that a large oscillation amplitude is reached. In addition, this flow configuration provides a strong influence on the fluid near the two sidewalls. In this experiment, the TR-PIV technique is employed to measure the velocity in at the midspan of the inverted flag. This TR-PIV system is mainly composed of 5-W continuous-wave semiconductor lasers (532 nm) and a 12-bit high-speed CMOS camera (Dimax HS4, PCO, USA) with  $2000 \times 1200$  pixels. The velocity fields are calculated by image pairs with standard cross-correlation algorithms. An interrogation window size of  $16 \times 16$  pixels with 50% overlap was applied in the measurements. A total of 20 000 instantaneous velocity fields were acquired from 20 001 successive images at a frame rate of 2000 Hz. The maximum particle displacement error in image pairs is less than 0.1 pixels, and so the uncertainty of the measurement is less than 2%. A more detailed description and further results of this experiment are available from Yu *et al.*<sup>13</sup>

#### B. Data acquisition

Motivated by the work of Tu *et al.*,<sup>8</sup> the procedures of data acquisition and separation were implemented using a similar strategy. The data acquisition procedure is aimed at establishing appropriate input and output datasets for the LSTM-based POD model. Given the oscillation frequency  $f_0 = 2.8$  Hz of the inverted flag, a frequency of  $f_p = 5$  Hz was selected as a sampling rate for non-TR-PIV measurement, which obviously cannot fulfill the requirements of the Nyquist-Shannon sampling theorem. This indicates that the non-TR flow at a low sampling rate is unable to resolve the time-scale characteristics as well as the TR flow. To fully leverage the original TR-PIV data, a downsampling procedure was conducted at different time steps of flow fields. This procedure can be regarded as simulating the procedure of repeating non-TR-PIV measurements at different time steps. Therefore, the 20 000 velocity fields can ultimately be downsampled into 400 samples, and each sample includes 50 velocity fields with a sampling rate of 5 Hz.

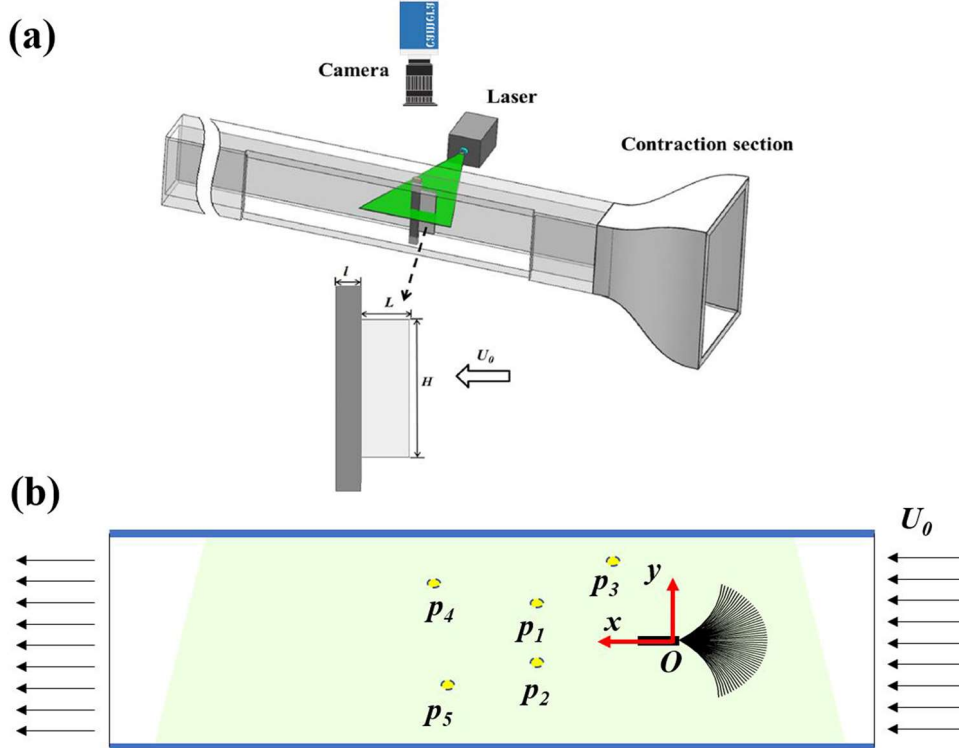


**FIG. 4.** (a) Diagram of the experimental setup. (b) Placement of five velocity sensors.

Discrete time-resolved velocity signals were obtained by extracting the streamwise velocity  $u$  from five points in the TR velocity fields. This procedure simulated the time-resolved velocity signals obtained using hot-wire probes. Similar to the procedure of generating non-TR-PIV data, the velocity signals can be downsampled to the same frequency and match the specific time step with the non-TR-PIV measurement. This procedure can facilitate the establishment of training datasets for the LSTM-based POD model. As shown in Fig. 4(b), two sensors ( $p_1$  and  $p_2$ ) are located at the two points of maximum  $u$ -velocity in the first mode (the most energetic mode), and two sensors ( $p_4$  and  $p_5$ ) are located at the center of large flow structures at the downstream in the first mode, and the last sensor ( $p_3$ ) is placed at the point of major fluctuation in the mean flow. The specific locations of the sensors are given in Fig. 4. The performance of the LSTM-based POD model is sensitive to the placement of the sensors. A detailed investigation of the sensitivity of the placement is beyond the scope of this work, but suggestions regarding the placement of sensors are given by Cole *et al.*<sup>29</sup> and Cohen *et al.*<sup>30</sup>

### C. Data separation and preprocessing

After acquiring and downsampling the original data, the data separation procedure was implemented to obtain the training dataset and the testing dataset for the LSTM-based POD model. In this study, 80 samples (4000 velocity flow fields in total) were randomly selected as a training dataset, while the rest of the 320 samples were used as a testing dataset. Although the training dataset is smaller than the testing dataset, the LSTM-based POD model still has acceptable performance. This can be attributed to the strong

relevance between inputs and outputs, as well as the outstanding learning ability of the LSTM-based POD model.

The POD coefficients were obtained by implementing the POD procedure on all the training and testing samples. The assumptions proposed by Tu *et al.*<sup>8</sup> were also applied here. It is assumed that the POD modes computed from the time-resolved velocity fields are the same as those obtained using randomly sampled velocity fields, especially when there are sufficient statistically independent snapshots. A simple validation was conducted, and the results show that the training datasets and testing datasets converge to the same eigenvalues after implementation of the POD procedure.

Data preprocessing is of great importance for the performance of neural networks. Without an appropriate data preprocessing method, the performance of the LSTM network would become somewhat unsatisfactory.<sup>22</sup> A common min-max normalization was implemented in data preprocessing as follows:

$$x' = (x - x_{\min}) / (x_{\max} - x_{\min}). \quad (11)$$

The normalization procedure was also implemented in the output datasets due to the enormous discrepancy in the coefficients of different POD modes. After data normalization, a procedure of data smoothing and noise reduction based on a multipoint average method was applied to the original velocity signals. The original signals directly extracted from the real flow contain abundant fluctuation terms and much experimental noise, which are difficult to capture by the reduced-order flow fields. Thus, the procedures of data preprocessing can improve the performance of the LSTM-based POD model to a certain extent.

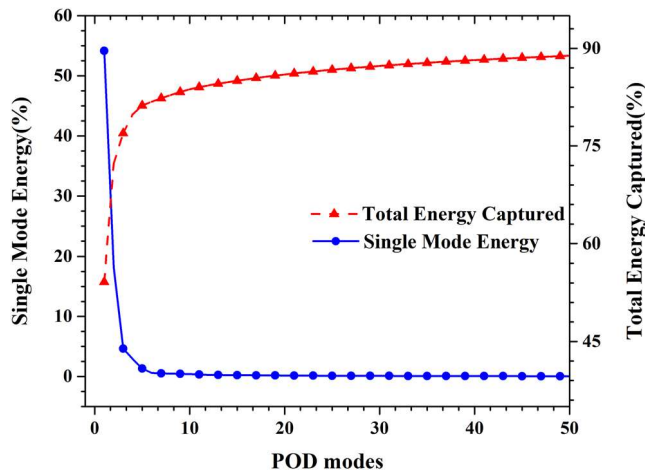


**FIG. 5.** Energy distribution and total energy captured by the first 50 POD modes.

#### IV. RESULTS AND DISCUSSION

##### A. Simple POD analysis

A simple POD analysis was conducted on the flow fields of an inverted flag oscillating in flapping mode to identify the dominant flow structures in this flow configuration. It is well accepted that the eigenvalue  $\lambda_i$  reflects a corresponding mode contribution to the turbulent kinetic energy (TKE). The percentage of energy  $\eta_i$  contained in each mode can be calculated as follows:

$$\eta_i = \frac{\lambda_i}{\sum_{j=1}^{N_t} \lambda_j} \times 100\%, \quad (12)$$

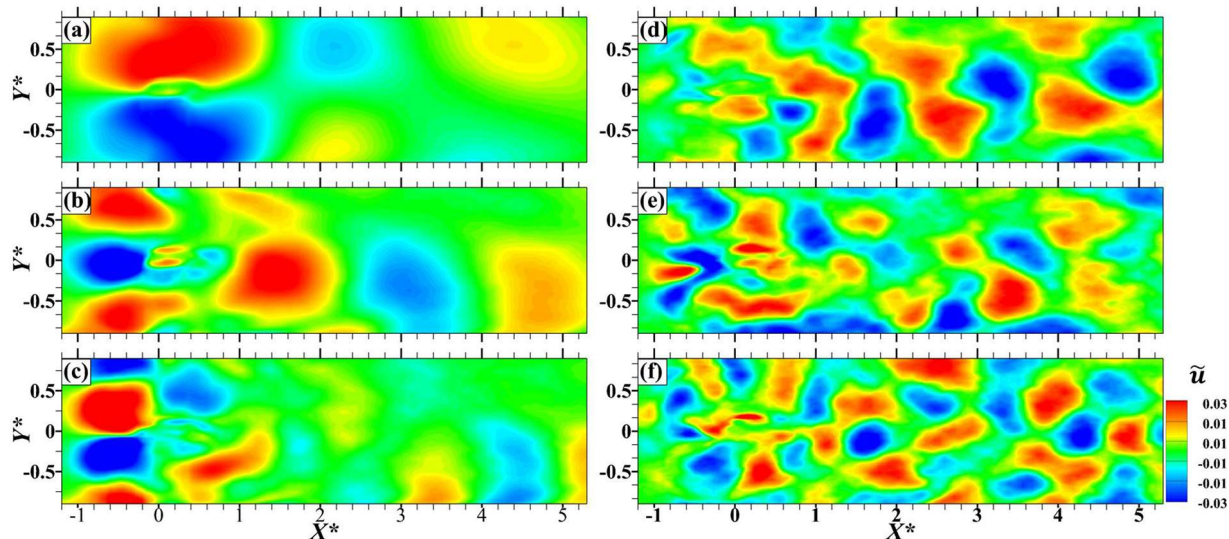
where  $N_t$  is the total number of POD modes.

Figure 5 shows the profiles of  $\eta_i$  with respect to the first 50 POD modes.  $\eta_i$  decreased quickly in the first 10 modes and then decreased gently. The bulk of the energy was contained in the first two POD modes, reaching 54% and 18%, respectively. However, the profile of the total energy captured displayed an opposite tendency. The first 10 modes contained 83% of the energy in the flow, while the 50 modes captured 89% in total. Although the last 40 POD modes merely captured 6% of the energy in total, the coefficients of these modes had great complexity, which can be utilized to test the learning ability and feasibility of the LSTM-based POD model. Therefore, the first 50 POD coefficients were selected as the outputs to investigate the performance of the model.

Figure 6 shows the different POD modes measured using the training dataset. In the contour plot of the first mode [Fig. 6(a)], two large-scale coherent structures were primarily observed near the inverted flag (located at  $X^* = 0$  and  $Y^* = 0$ ). These dominant flow structures were generated from the oscillation on the two sides of the inverted flag. The low-order POD [Figs. 6(a)–6(c)] modes containing the bulk of the TKE indicated that the majority of the large coherent structures existed in the upstream flow. The high-order POD modes [Figs. 6(d) and 6(e)] also contained small coherent structures with a relatively uniform distribution, but the physical significance is unclear.

##### B. Training error analysis

The learning capacity and robustness of the LSTM-based POD model were investigated by implementing different configurations of outputs in the model, as shown in Table I. The training error of the model was measured by the mean-square error between the real POD coefficients and the model outputs. In the following, “LSTM-POD-Mul” is used to represent the LSTM-based POD model with the multi-time-step structure, while “LSTM-POD-Sin” represents the one with the single-time-step structure.



**FIG. 6.** Contour plots of different POD modes obtained by the training dataset. (a) 1st mode, (b) 3rd mode, (c) 5th mode, (d) 25th mode, (e) 40th mode, and (f) 50th mode.

**TABLE I.** Comparison of training error at the last epoch in the LSTM-based POD model with different output configurations.

POD coefficient output	LSTM-POD-Mul	LSTM-POD-Sin
Modes 01~10	0.038 24	0.132 49
Modes 11~20	0.109 95	0.322 78
Modes 21~30	0.142 36	0.376 54
Modes 31~40	0.183 03	0.421 39
Modes 41~50	0.207 43	0.451 75

Figure 7 shows the profiles of the training error using different output configurations in the model. The 10 plotted curves show that as the number of epochs increased, the training error decreased rapidly for the first 1000 epochs, decreased gradually, and ultimately converged to a certain value. These converged values are displayed in Table I. However, a comparative study of LSTM-POD-Mul and LSTM-POD-Sin indicated significant differences in terms of convergence. As shown in Fig. 7 and Table I, LSTM-POD-Mul had a faster convergence rate and a lower convergence value and performed much better than LSTM-POD-Sin. This finding demonstrated that the multi-time-step configuration can facilitate the convergence of the model and augment the performance to a certain extent. In addition, the training error in the model that contained coefficients of high-order POD modes is much larger than that of the low-order counterparts. This can be attributed to the POD coefficients of high-order mode having great complexity and nonlinearity, which indicate a moderate correlation between the high-order POD coefficients and the velocity signals.

### C. POD coefficient reconstruction

The key to reconstructing the time-resolved flow fields is to recover the time-resolved POD coefficients as accurately as possible. This is also an essential indicator for evaluating the model performance. Figure 8 shows the time series of the coefficients in different

POD modes calculated using the LSTM-based POD model with different time-step configurations. Clear similarities were observed for both LSTM-POD-Mul (red lines) and LSTM-POD-Sin (blue lines). The coefficients obtained can capture the change of the POD coefficients in a real flow very well. There is no significant difference between the real POD coefficients and the coefficients generated by LSTM-POD-Mul/Sin in some low-order POD modes [Figs. 8(a)–8(c)]. What is surprising is that even the coefficients in some high-order POD modes [Figs. 8(d) and 8(e)] also have decent agreement with the real ones. This demonstrates that the LSTM-based models have great potential for addressing complicated time-series problems. However, it is notable that there is still some considerable error in the estimation outputs of the models that are inevitable, especially in high-order POD modes. This may be attributed to the great complexity and nonlinearity of the coefficients in high-order modes, which are somewhat unpredictable. In addition, the coefficients obtained using LSTM-POD-Sin (blue lines in Fig. 8) are a little unstable with small oscillation [Figs. 8(c)–8(e)]. A possible explanation is that LSTM-POD-Sin merely considered the data at the current time step, which may impact the continuity between data.

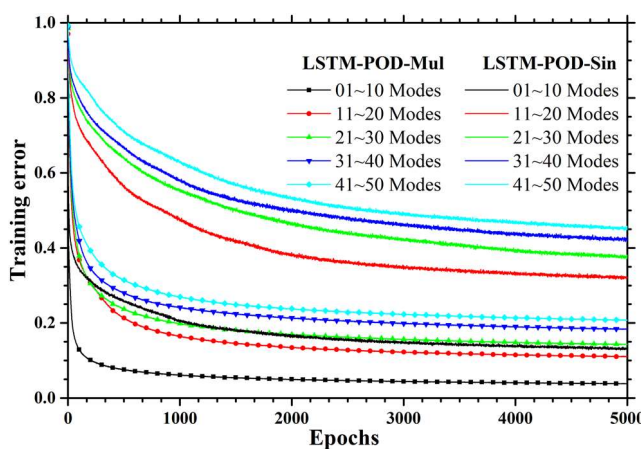
To further compare the performance of LSTM-POD-Mul and LSTM-POD-Sin, an error analysis of the POD coefficients was conducted, as shown in Fig. 9. In order to strengthen the comparability of the coefficients in different POD modes, the mean-squared error was calculated using coefficients that were normalized and scaled to the range of [0, 10]. The results demonstrate that the error of LSTM-POD-Sin (blue dashed line) is generally larger than that of LSTM-POD-Mul (red solid line). This indicates that LSTM-POD-Mul has better performance in POD coefficient reconstruction since it considers the temporal correlation between the time-series data.

Another interesting finding is that as the number of modes increased, the error rose in an oscillating way. Nevertheless, the error of most high-order modes was still larger than that of the low-order modes. This is consistent with the results and the analysis of the training error, which indicated that the correlation between coefficients of high-order POD modes and velocity signals is moderate and is thus more difficult to predict. However, the error in the high-order POD mode in this range is completely acceptable since the mode merely contributes a little energy to the flow.

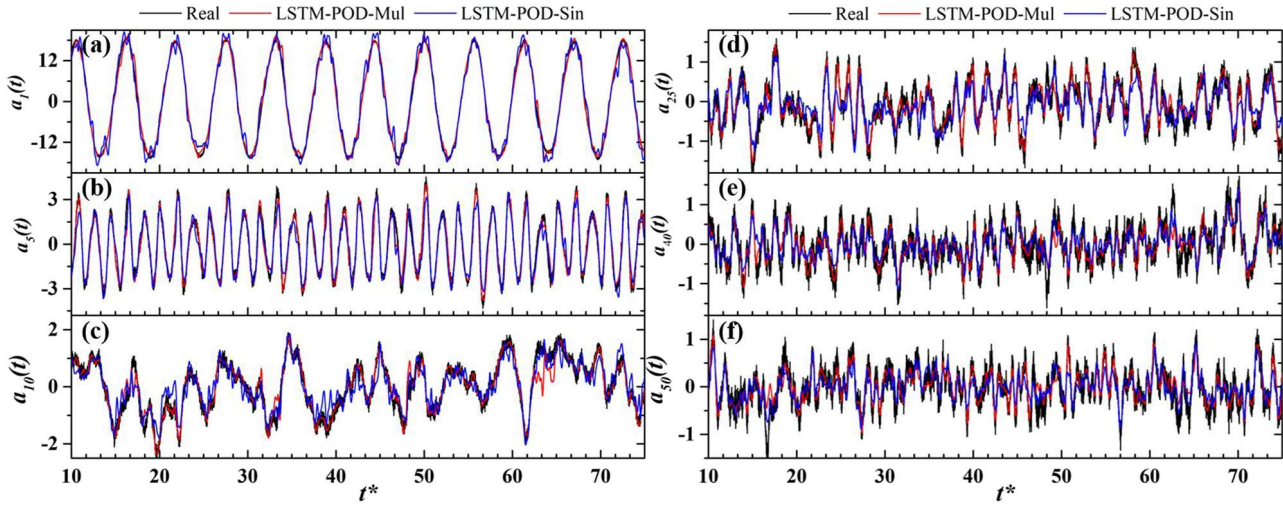
### D. Reduced-order flow field reconstruction

After the reconstruction of faithful time-resolved coefficients in different POD modes, the time-resolved reduced-order flow fields can be obtained using the POD reconstruction technique [Eq. (4)]. Figure 10 shows the time series of normalized velocity signals estimated using POD coefficients in a real flow or obtained from LSTM-POD-Mul/LSTM-POD-Sin. The velocity signals of three different discrete points were extracted from flow fields and compared, as shown in Fig. 10. The origin velocity signals in the real flow contained abundant fluctuation terms and much experimental noise, which cannot be captured by the reduced-order flow fields. Therefore, to enhance the comparability, the data preprocessing procedure described in Sec. III C was applied to all the velocity signals.

As shown in Fig. 10, there are enormous differences between the downsampled velocity signals (displayed as U-down with the dashed line) and the original velocity extracted from real flow fields



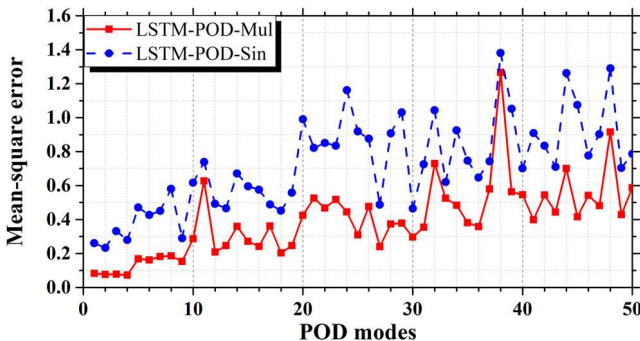
**FIG. 7.** Training error curves using different output configurations in the LSTM-based POD model.



**FIG. 8.** Time-series of the coefficients in different POD modes calculated with different LSTM model structures. The coefficients of (a) 1st mode, (b) 5th mode, (c) 10th mode, (d) 25th mode, (e) 40th mode, and (f) 50th mode.

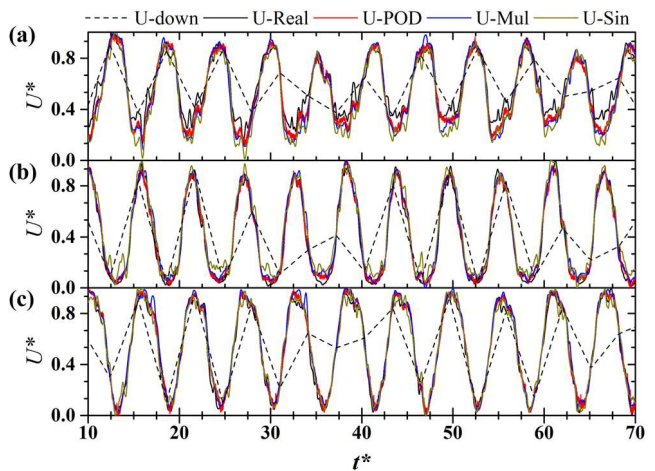
(displayed as U-POD with the dark line). This indicated that the downsampled velocity signals extracted from the flow fields of non-TR-PIV measurements cannot capture the variation in a fine time scale. However, for the other time-resolved velocity signals, no significant differences could be found. There is only a slight difference between the original velocity extracted from real flow fields and the velocity estimated using different POD-based models from the reduced-order flow fields. This can be explained by the energy wastage in reduced-order flow fields. Additionally, the velocity signals estimated by LSTM-POD-Mul (displayed as U-Mul with the blue line) or LSTM-POD-Sin (displayed as U-Sin with the brown line) are consistent with those estimated using POD coefficients in the real flow (displayed as U-POD with the red line). Based on these findings, it can be concluded that, in addition to near-perfect reconstruction of the time-series of POD coefficients, the proposed LSTM-based POD model is capable of accurately reconstructing time-resolved velocity signals.

Figure 11 shows the contour plots of two arbitrary instantaneous streamwise velocities in the training samples of the real flow



**FIG. 9.** Mean-squared error between the real POD coefficients and coefficients estimated using LSTM-based POD models in different POD modes.

[Fig. 11(a)]. These were reconstructed using real POD coefficients [Fig. 11(b)], coefficients estimated by LSTM-POD-Mul [Fig. 11(c)], and coefficients estimated by LSTM-POD-Sin [Fig. 11(d)]. The contours indicated that the large-scale flow structure can be readily captured by the flow fields reconstructed using POD coefficients. However, some significant differences were observed between the real flow [Fig. 11(a)] and the reduced-order flow [Figs. 11(b)–11(d)] since there are more flow details and finer-scale flow structures in the real flow. The difference in velocity magnitude between the real flow and the reduced-order flow is explained by the energy wastage of the



**FIG. 10.** Temporal resolution of three discrete point velocity signals recovered using the LSTM-based POD model with different time step configurations: (a)  $p_1$ , (b)  $p_2$ , and (c)  $p_3$ . U-down: the velocity extracted from the downsampling PIV fields at a sampling rate of 5Hz; U-real : the velocity extracted from the TR-PIV fields at a sampling rate of 2000Hz; U-POD: the velocity extracted from the reconstructed flow fields using real POD coefficients; U-Mul: the velocity extracted from the reconstructed flow fields using LSTM-POD-Mul model; U-Sin:the velocity extracted from the reconstructed flow fields using LSTM-POD-Sin model.

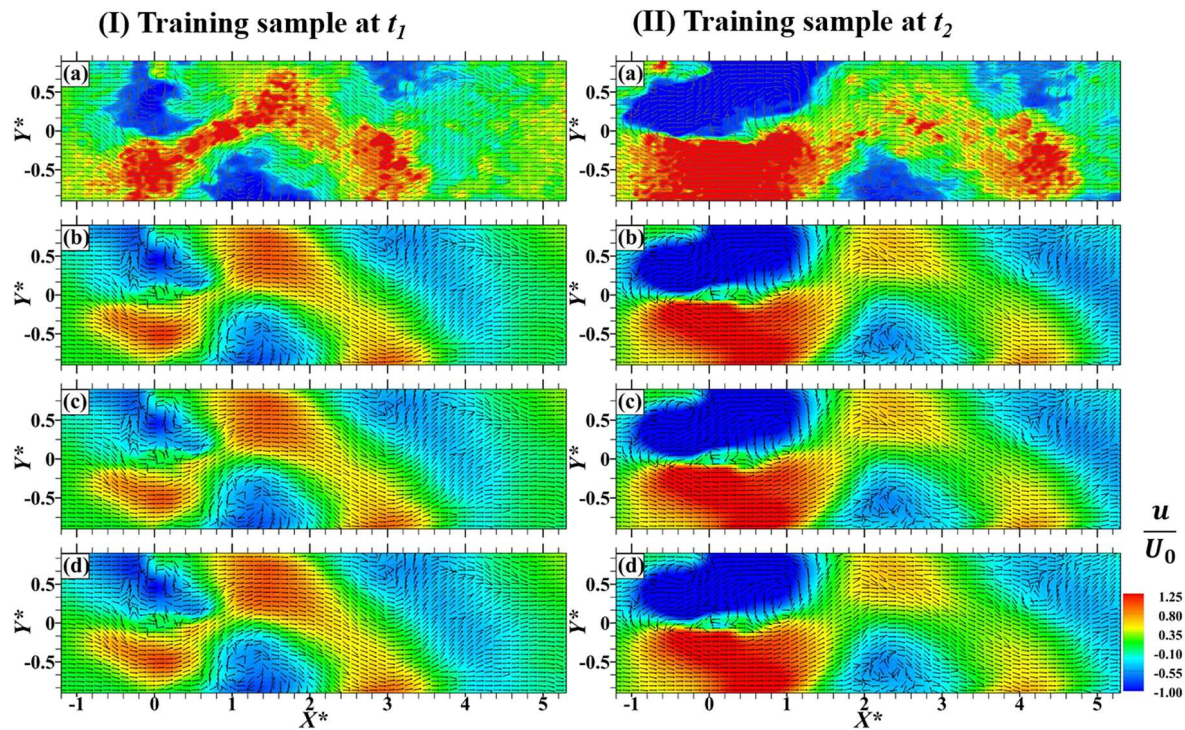


**FIG. 11.** Contour plots of the instantaneous streamwise velocity in training samples reconstructed using different LSTM-based POD models: (a) real flow, (b) real POD reconstruction, (c) LSTM-POD-Mul reconstruction, and (d) LSTM-POD-Sin reconstruction.

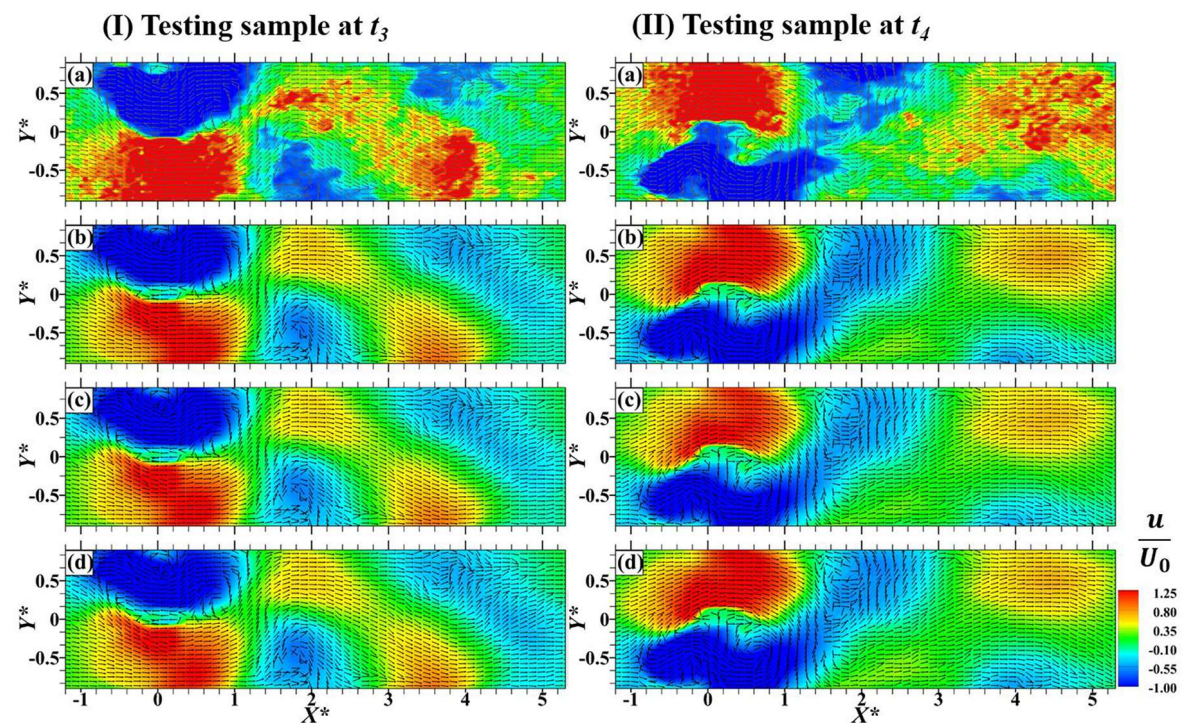


**FIG. 12.** Contour plots of the instantaneous streamwise velocity in testing samples reconstructed using different LSTM-based POD models: (a) real flow, (b) real POD reconstruction, (c) LSTM-POD-Mul reconstruction, and (d) LSTM-POD-Sin reconstruction.

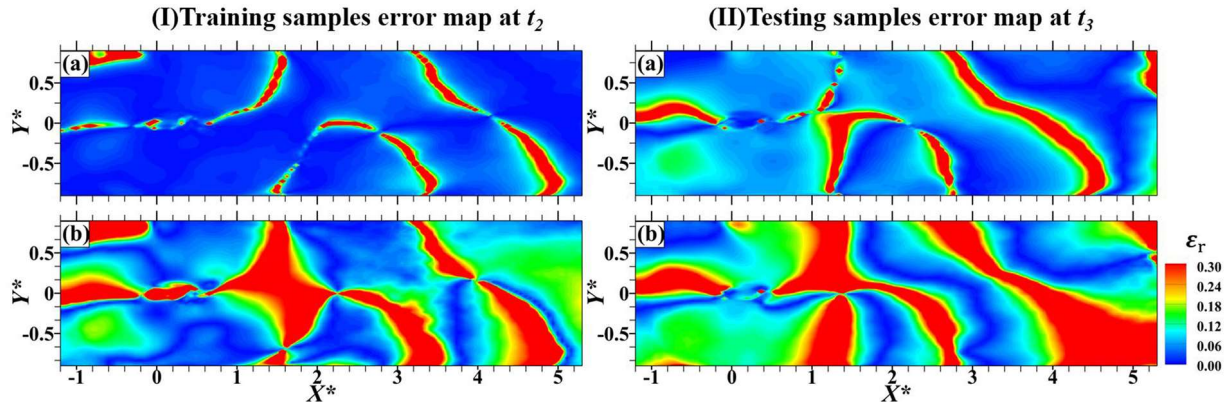


**FIG. 13.** The spatial distribution of the relative reconstruction error in training (I) and testing (II) samples: (a) real POD coefficients reconstruction vs LSTM-POD-Mul reconstruction and (b) real POD coefficients reconstruction vs LSTM-POD-Sin reconstruction.

POD reconstruction since the reduced-order flow fields only contained the energy of the leading 50 modes (89% in total). In contrast, the real flow fields contained the energy of the higher-order modes and a certain proportion of noise as well. Additionally, a comparative study of the flow fields reconstructed using LSTM-POD-Mul [Fig. 11(c)] and LSTM-POD-Sin [Fig. 11(d)] demonstrated that both models have similar performance upstream of the flow field and the primary differences stemmed from downstream of the flow field. The results show that the flow field reconstructed using LSTM-POD-Mul [Fig. 11(c)] is more analogous to that reconstructed using real POD coefficients [Fig. 11(b)]. This may be attributed to the better performance of LSTM-POD-Mul in the estimation of coefficients of high-order POD modes since these modes contained smaller coherent structures distributed downstream [Figs. 11(d)–11(f)].

The ultimate quality of reconstructed flow fields highly depends on the model performance on the testing samples. A striking result stems from the network's ability to recover the flow fields in the testing samples as faithfully as the training samples, as shown in Fig. 12. This indicated that the LSTM-based POD models have great learning and generalization ability. When it comes to the analysis of reconstructed results in testing samples, similar findings can be obtained, as mentioned in the training sample analysis.

### E. Relative reconstruction error analysis

A relative reconstruction error analysis was conducted to compare LSTM-POD-Mul and LSTM-POD-Sin, as shown in Fig. 13. The spatial distribution of the relative reconstruction error can be calculated as follows:

$$\epsilon_r = \sqrt{\frac{[u_l(x) - u_0(x)]^2}{u_0(x)^2}}, \quad (13)$$

where  $u_0$  and  $u_l$  are the velocity reconstructed using real POD coefficients and the velocity estimated using LSTM-POD-Mul or LSTM-POD-Sin, respectively. The error from LSTM-POD-Mul [Fig. 13(a)] is much smaller than that from LSTM-POD-Sin [Fig. 13(b)], which indicates that LSTM-POD-Mul performs much better. This is consistent with the results of the POD coefficient reconstruction

(Sec. IV C), which can account for the better reconstruction performance in LSTM-POD-Mul. Large relative error usually occurred near the margins of the large-scale flow structures since the velocity magnitude near the margins is very small and close to zero. Additionally, another finding in Fig. 13 is that the relative error in the training sample [Fig. 13(I)] is slightly less than that in the testing sample [Fig. 13(II)], which is quite a reasonable and common phenomenon for the machine learning algorithm.

### V. CONCLUDING REMARKS

The motivation of the present study was to recover the time-resolved turbulent flow fields from discrete point measurements and non-TR-PIV measurements using an LSTM-based artificial intelligence framework. To this end, an LSTM-based POD model was proposed to establish the relationship between the velocity signals of discrete points and the time-varying POD coefficients. The time-resolved flow fields can be successfully reconstructed using this model after training with a non-TR dataset. An inverted flag flow was selected as a benchmark configuration to demonstrate the performance and for comprehensive validation. The non-TR dataset at a sampling rate of 5 Hz was obtained by down-sampling the original time-resolved flow fields. Different time-step configurations were tested on the model to investigate its robustness and learning ability. In addition, a relative error analysis was conducted to investigate the feasibility of the reconstructed flow fields.

The results demonstrated that the framework has great learning ability and generalization in time-series reconstruction. The time-resolved coefficients in the first 50 POD modes can be successfully reconstructed to a great extent using the model. Striking results were obtained from the reconstruction of coefficients in high-order POD modes, which are complex and nonlinear. The time-resolved reduced-order flow fields can be obtained by combining POD coefficients and the corresponding modes. Notably, there are some acceptable and inevitable differences between the real flow fields and reduced-order flow fields, which can be attributed to the energy wastage of POD reconstruction. However, no significant differences were observed between the reduced-order flow fields reconstructed with real POD coefficients and those estimated using the

LSTM-based POD model. This indicated that the framework has great potential for applications in the field of turbulent flow control, where faithful reduced-order flow fields are needed.

In addition, the comparative study of LSTM-POD-Mul and LSTM-POD-Sin indicated that the model with the multi-time-step configuration can provide better performance with higher accuracy and lower relative reconstruction error. A possible explanation is that LSTM-POD-Sin merely considered the data at the current time step, while LSTM-POD-Mul considered the temporal correlation between the time-series data. Further research will concentrate on the adaptability of the proposed model in different flow configurations, such as nonperiodic flows. Data assimilation<sup>31</sup> techniques will also be implemented with the framework to further improve the model performance.

## ACKNOWLEDGMENTS

This research was supported by the International Research and Development Program of the National Research Foundation of Korea (NRF), which is funded by the Ministry of Science and ICT of Korea (Grant No. NRF-2017K1A3A1A30084513). Partial support was also obtained from the National Research Foundation of Korea (NRF) grant, which is funded by the Korean government (MSIT) (Grant Nos. 2011-0030013 and 2018R1A2B2007117).

## REFERENCES

- <sup>1</sup>P. J. Schmid, "Dynamic mode decomposition of numerical and experimental data," *J. Fluid Mech.* **656**, 5 (2010).
- <sup>2</sup>K. Fukami, K. Fukagata, and K. Taira, "Super-resolution reconstruction of turbulent flows with machine learning," *J. Fluid Mech.* **870**, 106 (2019).
- <sup>3</sup>Y. Xie, E. Franz, M. Chu, and N. Thuerey, "tempoGAN: A temporally coherent, volumetric GAN for super-resolution fluid flow," *ACM Trans. Graphics* **37**, 95 (2018).
- <sup>4</sup>J. N. Kutz, "Deep learning in fluid dynamics," *J. Fluid Mech.* **814**, 1 (2017).
- <sup>5</sup>X. Jin, P. Cheng, W.-L. Chen, and H. Li, "Prediction model of velocity field around circular cylinder over various Reynolds numbers by fusion convolutional neural networks based on pressure on the cylinder," *Phys. Fluids* **30**, 047105 (2018).
- <sup>6</sup>V. Sekar, Q. Jiang, C. Shu, and B. C. Khoo, "Fast flow field prediction over airfoils using deep learning approach," *Phys. Fluids* **31**, 057103 (2019).
- <sup>7</sup>L. Zhu, W. Zhang, J. Kou, and Y. Liu, "Machine learning methods for turbulence modeling in subsonic flows around airfoils," *Phys. Fluids* **31**, 015105 (2019).
- <sup>8</sup>J. H. Tu, J. Griffin, A. Hart, C. W. Rowley, L. N. Cattafesta, and L. S. Ukeiley, "Integration of non-time-resolved PIV and time-resolved velocity point sensors for dynamic estimation of velocity fields," *Exp. Fluids* **54**, 1429 (2013).
- <sup>9</sup>R. Leroux, L. Chatellier, and L. David, "Time-resolved flow reconstruction with indirect measurements using regression models and Kalman-filtered POD ROM," *Exp. Fluids* **59**, 16 (2018).
- <sup>10</sup>C. He and Y. Liu, "Proper orthogonal decomposition-based spatial refinement of TR-PIV realizations using high-resolution non-TR-PIV measurements," *Exp. Fluids* **58**, 86 (2017).
- <sup>11</sup>R. Swischuk, L. Mainini, B. Peherstorfer, and K. Willcox, "Projection-based model reduction: Formulations for physics-based machine learning," *Comput. Fluids* **179**, 704 (2019).
- <sup>12</sup>A. T. Mohan and D. V. Gaitonde, "A deep learning based approach to reduced order modeling for turbulent flow control using LSTM neural networks," preprint [arXiv:1804.09269](https://arxiv.org/abs/1804.09269) (2018).
- <sup>13</sup>Y. Yu, Y. Liu, and Y. Chen, "Vortex dynamics behind a self-oscillating inverted flag placed in a channel flow: Time-resolved particle image velocimetry measurements," *Phys. Fluids* **29**, 125104 (2017).
- <sup>14</sup>G. Berkooz, P. Holmes, and J. L. Lumley, "The proper orthogonal decomposition in the analysis of turbulent flows," *Annu. Rev. Fluid Mech.* **25**, 539 (1993).
- <sup>15</sup>J. L. Lumley, *Stochastic Tools in Turbulence* (Courier Corporation, 2007).
- <sup>16</sup>L. Sirovich, "Turbulence and the dynamics of coherent structures. I. Coherent structures," *Q. Appl. Math.* **45**, 561 (1987).
- <sup>17</sup>Q. Zhang and Y. Liu, "Influence of incident vortex street on separated flow around a finite blunt plate: PIV measurement and POD analysis," *J. Fluids Struct.* **55**, 463 (2015).
- <sup>18</sup>S. Hochreiter and J. Schmidhuber, "Long short-term memory," *Neural Comput.* **9**, 1735 (1997).
- <sup>19</sup>H. Sak, A. Senior, and F. Beaufays, "Long short-term memory recurrent neural network architectures for large scale acoustic modeling," In *INTERSPEECH 2014* (2014), pp. 338–342.
- <sup>20</sup>F. A. Gers and E. Schmidhuber, "LSTM recurrent networks learn simple context-free and context-sensitive languages," *IEEE Trans. Neural Networks* **12**, 1333 (2001).
- <sup>21</sup>F. A. Gers, D. Eck, and J. Schmidhuber, *Applying LSTM to Time Series Predictable Through Time-Window Approaches* (Springer, 2002).
- <sup>22</sup>A. Graves, *Long Short-Term Memory* (Springer, 2012).
- <sup>23</sup>S. Ioffe and C. Szegedy, "Batch normalization: Accelerating deep network training by reducing internal covariate shift," preprint [arXiv:1502.03167](https://arxiv.org/abs/1502.03167) (2015).
- <sup>24</sup>S. Han, H. Mao, and W. J. Dally, "Deep compression: Compressing deep neural networks with pruning, trained quantization and Huffman coding," preprint [arXiv:1510.00149](https://arxiv.org/abs/1510.00149) (2015).
- <sup>25</sup>C. Ledig, L. Theis, F. Huszár, J. Caballero, A. Cunningham, A. Acosta, A. Aitken, A. Tejani, J. Totz, and Z. Wang, "Photo-realistic single image super-resolution using a generative adversarial network," in *Proceedings of the IEEE Conference on Computer Vision and Pattern Recognition* (IEEE, 2017), pp. 4681–4690.
- <sup>26</sup>D. P. Kingma and J. Ba, "Adam: A method for stochastic optimization," preprint [arXiv:1412.6980](https://arxiv.org/abs/1412.6980) (2014).
- <sup>27</sup>M. Abadi, P. Barham, J. Chen, Z. Chen, A. Davis, J. Dean, M. Devin, S. Ghemawat, G. Irving, and M. Isard, "Tensorflow: A system for large-scale machine learning," in *Proceedings of the 12th USENIX Symposium on Operating Systems Design and Implementation (OSDI '16)* (USENIX, 2016), pp. 265–283.
- <sup>28</sup>F. Chollet, *Keras*, 2015.
- <sup>29</sup>D. R. Cole, M. N. Glauser, and Y. G. Guezenne, "An application of the stochastic estimation to the jet mixing layer," *Phys. Fluids A* **4**, 192 (1992).
- <sup>30</sup>K. Cohen, S. Siegel, and T. McLaughlin, "A heuristic approach to effective sensor placement for modeling of a cylinder wake," *Comput. Fluids* **35**, 103 (2006).
- <sup>31</sup>G. Evensen, *Data Assimilation: The Ensemble Kalman Filter* (Springer-Verlag New York, Inc., 2006).